

Disorder-dependent superconductivity, Berry-phase and bulk Fermi-surface of the Weyl type-II semi-metal candidate MoTe₂

D. Rhodes^{†,1,2} Q. Zhou^{†,1,2} R. Schönemann^{1,3} Q. R. Zhang^{1,2} E. Kampert³ Y.-c. Chiu^{1,2} Y. Lai^{1,2} Y. Shimura^{1,4} G. T. McCandless⁵ J. Y. Chan⁵ D. W. Paley^{6,7} J. Lee⁸ J. P. C. Ruff⁸ S. Das^{1,2} E. Manousakis^{2,1} M. D. Johannes⁹ and L. Balicas^{1,*}

¹National High Magnetic Field Laboratory, Florida State University, Tallahassee-FL 32310, USA

²Department of Physics, Florida State University, Tallahassee-FL 32306, USA

³Dresden High Magnetic Field Laboratory (HLD-EMFL),

Helmholtz-Zentrum Dresden-Rossendorf, 01328 Dresden, Germany

⁴University of Tokyo, Institute of Solid State Physics, Kashiwa, Chiba 2778581, Japan

⁵The University of Texas at Dallas, Department of Chemistry and Biochemistry, Richardson, TX 75080 USA

⁶Department of Chemistry, Columbia University, New York, NY 10027 USA

⁷Columbia Nano Initiative, Columbia University, New York, NY 10027 USA

⁸CHESS, Cornell University, Ithaca, New York 14853, USA

⁹Center for Computational Materials Science, Naval Research Laboratory, Washington, DC 20375, USA

(Dated: April 7, 2017)

The electronic structure of semi-metallic transition-metal dichalcogenides, such as WTe₂ and orthorhombic γ -MoTe₂, are claimed to be characterized by a Z_2 topological invariant. In addition, their Fermi surfaces are predicted to contain pairs of Weyl points or linearly touching electron and hole pockets associated with a non-trivial Chern number. For this reason, these compounds were recently claimed to conform to a new class, deemed type-II, of Weyl semi-metallic systems. A series of very recent angle resolved photoemission experiments (ARPES) claim to display a broad agreement with these predictions detecting, for example, topological Fermi arcs at the surface of the crystals. We synthesized single-crystals of semi-metallic MoTe₂ through a Te flux method in an attempt to validate these predictions through measurements of its bulk Fermi surface (FS) *via* quantum oscillatory phenomena. We find that its superconducting transition temperature depends on disorder as quantified by the ratio between the room- and low-temperature resistivities, suggesting the possibility of an unconventional superconducting pairing symmetry. Similarly to WTe₂, its magnetoresistivity does not saturate at high magnetic fields and can easily surpass 10⁶ %. Remarkably, the analysis of the quantum oscillatory signal superimposed onto the magnetic susceptibility, as extracted from the measurements of the magnetic torque, indicates that the geometry of the Fermi surface (FS) is markedly distinct from the calculated one and hence from the one revealed by ARPES. Furthermore, the de Haas van Alphen signal clearly reveals that the FS is affected by the Zeeman-effect which precludes the extraction of the Berry phase. Anomalies seen in the heat-capacity and in the Hall-effect indicate that the crystallographic and the electronic structures γ -MoTe₂ evolve upon cooling below 100 K, which is the temperature used to extract the crystallographic structure introduced into the reported calculations. Synchrotron single-crystal X-ray diffraction measurements confirm that the structure continues to evolve below 100 K which could partially explain the discrepancy between the calculations and our measurements.

Keywords: Subject Areas: Condensed Matter Physics, Superconductivity

I. INTRODUCTION

Transition-metal dichalcogenides (TMDs) belonging to the orthorhombic and non-centrosymmetric $Pmn2_1$ space group, e.g. WTe₂, were recently claimed to be characterized by a non-trivial $Z_2 = 1$ topological invariant based on the parity of their valence bands, making them good candidates for a quantum spin Hall insulating ground-state [1]. This state is characterized by helical edge states that are protected by time-reversal symmetry from both localization and elastic backscattering. Hence, these compounds would provide a platform for realizing low dissipation quantum electronics and spintronics [1, 2].

However, the majority of gapped TMDs such as semi-conducting MoS₂ or WSe₂, crystallize either in a trigonal prismatic coordination or in a triclinic one [3, 4] as ReS₂. Those crystallizing in the aforementioned orthorhombic phase, e.g. WTe₂, are semi-metals albeit displaying anomalous transport properties such as an enormous non-saturating magnetoresistivity [5]. However, strain is predicted to open a band gap [1] in WTe₂ which would make it suitable for device development. In fact, simple exfoliation of its isostructural MoTe₂ compound into thin atomic layers is claimed to induce a band gap [6] in absence of strain. Such a transition would contrast with band structure calculation predictions which find that it should remain semi-metallic when exfoliated down to a single atomic layer [7]. In fact, the insulating behavior reported for a few atomic layers of WTe₂ was ascribed to an increase in disorder due to its chemical

* balicas@magnet.fsu.edu

instability in the presence of humidity which is claimed to induce Anderson localization [8].

Orthorhombic MoTe_2 and its isostructural compound WTe_2 were also claimed recently to belong to a new class of Weyl semi-metals (i.e. type II) characterized by a linear touching between hole and electron Fermi surfaces [9–11] in addition to nodal lines [11]. Here, motivated by the scientific relevance and the technological implications of the aforementioned theoretical predictions [1, 9–11] we evaluate, through electrical transport and torque magnetometry, the electronic structure at the Fermi level of bulk single-crystals of orthorhombic MoTe_2 and its topological nature. Our goal is to contrast our experimental observations with the theoretical expectations and the ARPES results in order to support their findings and to provide relevant information that would help us predict the electronic properties of heterostructures fabricated from single- or few atomic layers of this compound. An agreement between the calculated geometry of the Fermi surface of MoTe_2 with the one extracted from quantum oscillatory phenomena, would unambiguously support the existence of Weyl nodes in the bulk [12] and therefore the existence of related non-trivial topological surface states, or Fermi arcs [13, 14] in single or few-atomic layers [9–11]. Although quantum oscillatory phenomena supports the notion of a non-trivial Berry phase for the bulk electronic structure of orthorhombic MoTe_2 , we unexpectedly find that the geometry of its Fermi surface differs considerably from the calculated one. Therefore, we conclude that these predictions should be revisited once the low temperature crystallographic structure of MoTe_2 is determined.

II. METHODS AND EXPERIMENTAL RESULTS

Very high quality single crystals of monoclinic β - MoTe_2 were synthesized through a Te flux method: Mo, 99.9999%, and Te 99.9999 % powders were placed in a quartz ampoule in a ratio of 1:25. Subsequently, the material was heated up to 1050 °C and held at this temperature for 1 day. Then, the ampoule was slowly cooled down to 900 °C and centrifuged. The “as harvested” single-crystals were subsequently annealed for a few days at a temperature gradient to remove the excess Te. Magneto-transport measurements as a function of temperature were performed in a Physical Property Measurement System using a standard four-terminal configuration. Measurements of the Shubnikov-de-Haas (SdH) and the de-Haas-van-Alphen (dHvA) effects were performed in dilution refrigerator coupled to a resistive Bitter magnet, with the samples immersed in the ^3He - ^4He mixture. Measurements of the dHvA-effect were performed *via* a torque magnetometry technique, i.e. by measuring the deflection of a Cu-Be cantilever capacitively. Electrical transport measurements in pulsed magnetic fields were performed at the Dresden High Mag-

netic Field Laboratory using a 62 T magnet with a pulse duration of 150 ms. The sample temperature was controlled using a ^4He bath cryostat (sample in He atmosphere) with an additional local heater for temperatures above 4.2 K. Synchrotron based X-ray measurements were performed at CHESS-A2 beam line, using 19.9 keV photons (with an energy bandwidth of ~ 2 eV). Two single-crystals were measured. The first crystal, or sample 1, has dimensions of $\sim 100 \times 30 \times 10 \mu\text{m}^3$, and was fully bathed by a nitrogen gas jet when subjected to the $200 \times 200 \mu\text{m}^2$ incident beam. For sample 2, the incident beam was reduced to $80 \times 80 \mu\text{m}^2$ in to illuminate fewer grains from a larger crystal (few mm long) characterized by significant structural disorder. The temperature of this sample was controlled using a closed-cycle cryostat. The diffracted X-rays were recorded using a Pilatus3 300 K area detector mounted on the 2θ arm of a 4-circle diffractometer.

As illustrated by Fig. 1(a), the “as synthesized” single-crystals display resistivity ratios $RRR = \rho(T = 300 \text{ K})/\rho(T = 2 \text{ K})$ ranging from 380 to > 2000 which is one to two orders of magnitude higher than RRR values currently available in the literature (see, for example, Ref. 15). Although not clearly visible in Fig. 1(a) due to its logarithmic scale, a hysteretic anomaly is observed in the resistivity around 240 K which corresponds to the monoclinic to orthorhombic structural transition which stabilizes what we denominate as the orthorhombic γ - MoTe_2 phase. See, Ref. 16 for a clearer exposure of this transition and related hysteresis. These single-crystals were subsequently measured at much lower temperatures allowing us determine their superconducting transition temperature T_c . Remarkably, and as seen in Fig. 1(b), we find that T_c depends on sample quality, increasing considerably as the RRR increases, suggesting that structural disorder suppresses T_c . For these measurements, particular care was taken to suppress the remanent field of the superconducting magnet since the upper critical fields are rather small, see Supplemental Fig. S1 [17]. The sample displaying the highest RRR and concomitant T_c was measured in absence of a remanent field. To verify that these differences in T_c are not due to a poor thermal coupling between the sample and the thermometers, T_c was measured twice by increasing and decreasing T very slowly. The observed hysteresis is small relative to T_c indicating that the measured T_c s are not an artifact. The values of the residual resistivities ρ_0 depend on a careful determination of the geometrical factors such as the size of the electrical contacts. Therefore, the RRR provide a more accurate determination of the single-crystalline quality. In the past, the suppression of T_c by impurities and structural defects was systematically taken as evidence for unconventional superconductivity [18–20], e.g. triplet superconductivity [21] in Sr_2RuO_4 . As discussed below, the current lack of a clear understanding on the electronic structure of γ - MoTe_2 prevents us from providing a reasonable scenario for its pairing symmetry. Nevertheless, the fittings of

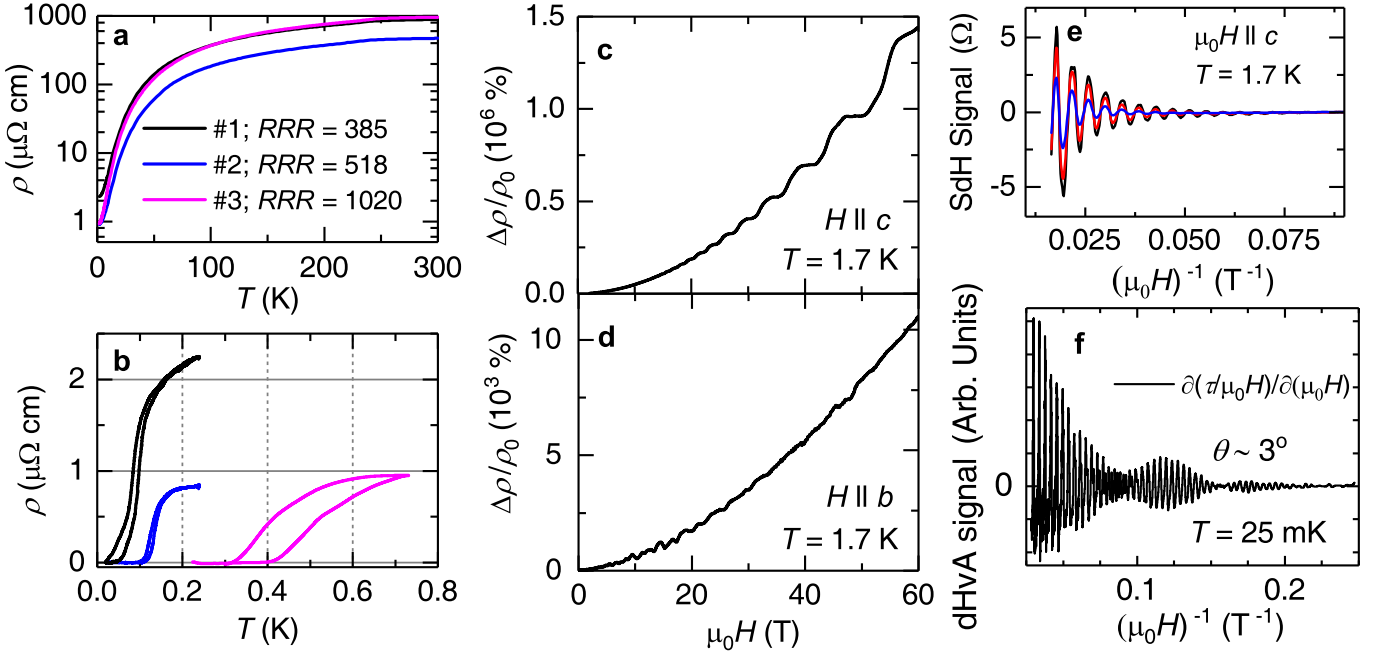


FIG. 1. (a) Resistivity ρ , for currents flowing along the a -axis, as a function of the temperature T for three representative single crystals displaying resistivity ratios $\rho(300\text{ K})/\rho(2\text{ K})$ between 380 and ~ 1000 . (b) ρ as a function of T for each single-crystal indicating that T_c depends on sample quality. The apparent hysteresis is due to a non-ideal thermal coupling between the single-crystals, the heater and the thermometer. (c) ρ as a function of the field H applied along the c -axis at a temperature $T = 1.7\text{ K}$. Notice i) the non-saturation of $\rho(H)$ and ii) that $\Delta\rho(\mu_0 H)/\rho_0 = (\rho(\mu_0 H) - \rho_0)/\rho_0$, where $\rho_0 = \rho(\mu_0 H = 0\text{ T}, T = 2\text{ K})$ surpasses $1.4 \times 10^6\%$ at $\mu_0 H = 60\text{ T}$. (d) ρ as a function of $\mu_0 H$ applied along the b -axis also at $T = 1.7\text{ K}$ and for the same single-crystal. (e) Shubnikov de Haas signal superimposed onto the magnetoresistivity for $\mu_0 H \parallel c$ -axis and for three temperatures, $T = 8\text{ K}$ (blue line), 4.2 K (red line) and 1.7 K (black line), respectively. (f) Oscillatory signal (black line) superimposed onto the magnetic susceptibility $\Delta\chi = \partial(\tau/\mu_0 H)/\partial\mu_0 H$, where τ is the magnetic torque. Red line is a fit to four Lifshitz-Kosevich oscillatory components, i.e. two fundamental frequencies plus their harmonics, from which one extracts the respective Berry phases.

the upper-critical fields H_{c2} to a conventional Ginzburg-Landau expression, see Fig. S1 [17], points towards singlet pairing.

Figures 1(c) and 1(d) display the change in magnetoresistivity $\Delta\rho(\mu_0 H)/\rho_0 = (\rho(\mu_0 H) - \rho_0)/\rho_0$ as a function of the field $\mu_0 H$ for a crystal characterized by $RRR \sim 450$ when the electrical current flows along the crystalline a -axis and the field is applied either along the c - or the b -axes, respectively. Similarly to WTe_2 , for both orientations $\Delta\rho/\rho_0$ shows no sign of saturation under fields all the way up to 60 T while surpassing $1 \times 10^6\%$ for $\mu_0 H \parallel c$ -axis [5]. For WTe_2 such anomalous magnetoresistivity was attributed to compensation between the density of electrons and holes [5, 22, 23]. Nevertheless, there are a number of subsequent observations[24] contradicting this simple scenario such as i) a non-linear Hall response [25], ii) the suppression of the magnetoresistivity at a pressure where the Hall response vanishes[26] (i.e. at perfect compensation) and iii) the observation of a pronounced magnetoresistivity in electrolyte gated samples with a considerably higher density of electrons with respect to that of holes [27]. It remains unclear if the proposed unconventional electronic structure [9–11] would play a role on

the giant magnetoresistivity of WTe_2 , while its measured Fermi surface differs considerably from the calculated one [24]. In contrast, we have previously shown that $\gamma\text{-MoTe}_2$ indeed is a well compensated semi-metal [16].

The best samples, i.e. those with $RRR \geq 2000$, display even more pronounced $\Delta\rho/\rho_0$ under just $\mu_0 H \simeq 10\text{ T}$. The oscillatory component superimposed on the magnetoresistivity corresponds to the Shubnikov-de Haas (SdH) effect resulting from the Landau quantization of the electronic orbits. Figure 1(e) shows the oscillatory, or the SdH signal as a function of inverse field $(\mu_0 H)^{-1}$ for three temperatures. The SdH signal was obtained by fitting the background signal to a polynomial and then by subtracting it. Notice how for this sample and for this orientation, that is for $\mu_0 H \parallel c$ -axis, the SdH signal is dominated by a single frequency. However for all subsequent measurements performed under continuous fields (discussed below) one observes the presence of two close frequencies, each associated to a extremal cross-sectional area A of the Fermi surface through the Onsager relation $F = A(\hbar/2\pi e)$ where \hbar is the Planck constant and e is the electron charge. To illustrate this point we show in Fig. 1(f) the oscillatory signal extracted from the mag-

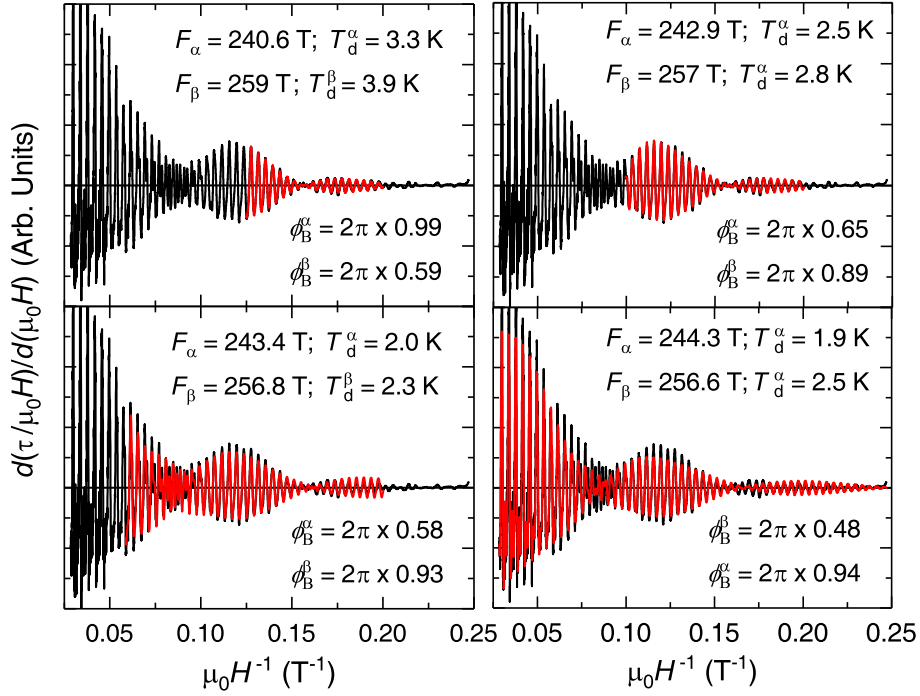


FIG. 2. (a) From left to right and from top to bottom: fits (red lines) of the de Haas van Alphen signal superimposed onto the magnetic susceptibility (as extracted from the derivative of the magnetic torque τ with respect to $\mu_0 H$) to four Lifshitz-Kosevich oscillatory components. The four components describe the two fundamental frequencies F_α and F_β observed for fields applied along the c -axis along with their first harmonics. Notice that the fundamental frequencies shift as the interval in $(\mu_0 H)^{-1}$ increases. The obtained Berry phases $\phi_B^{\alpha,\beta}$ and extracted Dingle temperatures $T_d^{\alpha,\beta}$ are also field-dependent. Hence, the electronic structure of γ -MoTe₂ is affected by the Zeeman-effect which prevents the extraction of its Berry phase.

netic torque, i.e. $\tau = \mathbf{M} \times \mu_0 \mathbf{H}$, or the de Haas van Alphen effect (dHvA) collected from a γ -MoTe₂ single-crystal for fields aligned nearly along its c -axis. Here $M = \chi \mu_0 H$ is the sample's magnetization and $\chi(\mu_0 H, T)$ is its magnetic susceptibility. Actually, Fig. 1(f) displays the oscillatory component of the magnetic susceptibility $\Delta\chi = \partial(\tau/\mu_0 H)/\partial(\mu_0 H)$. The envelope of the oscillatory signal shows the characteristic “beating” pattern between two close frequencies as shown in its fast Fourier transform shown further below in this manuscript.

In Figure 2 we display this oscillatory signal as function of $(\mu_0 H)^{-1}$ along with fits to four Lifshitz-Kosevich oscillatory components performed over an increasing range in $(\mu_0 H)^{-1}$. Two of these components describe the fundamental frequencies while the other two depict their first harmonics, respectively. The objective of these fits is to evaluate the Berry-phase and therefore the topological character of γ -MoTe₂. In effect, according to The Lifshitz-Onsager quantization condition [28, 29] the oscillatory component superimposed onto the susceptibility is given by:

$$\Delta\chi[(B)^{-1}] \propto \frac{T}{B^{5/2}} \sum_{l=1}^{\infty} \frac{\exp^{-l\alpha\mu T_D/B} \cos(lg\mu\pi/2)}{l^{3/2} \sinh(\alpha\mu T/B)} \times \cos \left\{ 2\pi \left[\left(\frac{F}{B} - \frac{1}{2} + \phi_B \right) l \pm \delta \right] \right\} \quad (1)$$

where F is the dHvA frequency, l is the harmonic index, ω_c the cyclotron frequency, g the Landé g -factor, μ the effective mass in units of the free electron mass m_0 , and α is a constant. δ is a phase shift determined by the dimensionality of the Fermi surface which acquires a value of either $\delta = 0$ or $\pm 1/8$ for two- and three-dimensional Fermi surfaces, respectively. ϕ_B is the Berry phase which, for Dirac and Weyl systems, is predicted to acquire a value $\phi_B = \pi$. Finally, $T_D = \hbar/(2\pi k_B \tau)$ is the so-called Dingle temperature from which one extracts τ or the characteristic quasiparticle scattering time.

As seen through the four panels in Fig. 2, one obtains $F_\alpha = 240.4$ T and $F_\beta = 259$ T for the fundamental frequencies and for fields below 10 T, but they are observed to continuously evolve as the field interval is increased, i.e. F_α increases to 244.3 T while F_β decreases slightly to 256.6 T when one fits the entire fit range. Meanwhile, and assuming constant values for the effective masses (extracted below), one observes the Dingle temperatures to decrease as the fit progressively includes the whole field range. For example, T_D^α decreases from 3.3 K to 1.9 K. Similarly, the phase-factors from which one extracts the Berry phases $\phi_B^{\alpha,\beta}$ are also found to be strongly field-dependent. The values of $\phi_B^{\alpha,\beta}$ indicated in the figure were calculated assuming maxima extremal-cross-sectional areas and a three-dimensional FS. As discussed

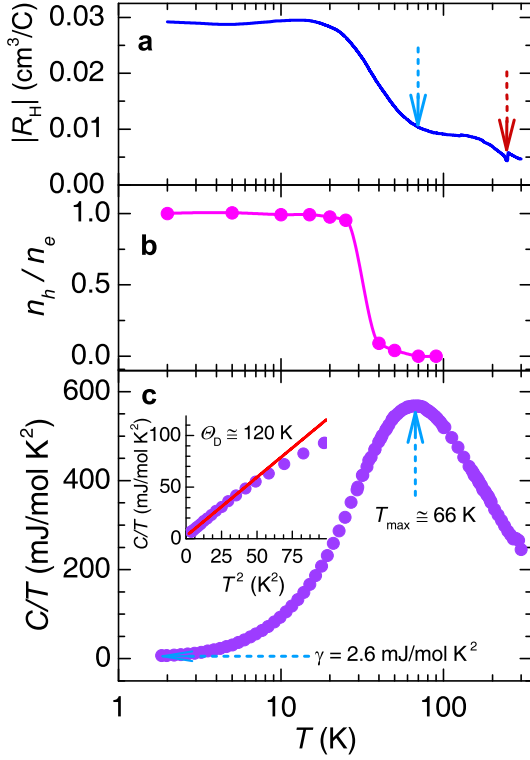


FIG. 3. (a) Absolute value of the Hall constant $|R_H|$ measured under a field $H = 9$ T as a function of the temperature. Brown arrow indicates the temperature $T \sim 240$ K where the monoclinic to orthorhombic transition occurs. Blue arrow indicates the temperature below which a sharp increase is observed in the Hall response, suggesting a crossover or a possible electronic phase-transition. (b) Ratio between the density of holes n_h and the density of electrons n_e as a function of T and as extracted from a two-band analysis of the Hall-effect. Notice how n_h increases very quickly below 40 K reaching parity with n_e below ~ 15 K. Hence, the Hall-effect indicates that this compound becomes nearly perfectly compensated at low temperatures. (c) Heat capacity C normalized by the temperature T and as a function of T for a β, γ -MoTe₂ single-crystal. A broad anomaly is observed at $T_{\text{max}} \simeq 66$ K around which μ_h is seen to increase abruptly. At low T s, C/T saturates at $\gamma \simeq 2.6$ mJ/mol K^2 which corresponds to the electronic contribution to C/T . Inset: C/T as a function of T^2 . Red line is a linear fit from which one extracts the phonon coefficient ϑ in $C/T \propto \vartheta T^3$ which yields a Debye temperature $\Theta_D \simeq 120$ K.

in great detail below, our quantum oscillatory study on the geometry of the Fermi surfaces (FS) of γ -MoTe₂ indicates that all of its FSs are three-dimensional in character, in contrast to band structure calculations. Hence, δ should acquire values of $\pm 1/8$. However, Hall-effect measurements in γ -MoTe₂ indicates that it is a compensated semi-metal at low temperatures [16]. This implies that each of the two frequencies, or FS cross-sectional-areas observed for $H \parallel c$ -axis, should be attributed to one electron- and one hole-pocket, respectively. Therefore, these orbits must correspond to maxima FS cross-

sectional-areas and therefore δ should acquire a value of $-1/8$, see Ref. 30. To summarize, the geometry of the Fermi surface of γ -MoTe₂ evolves as the field increases due to the Zeeman-effect which precludes the extraction of its Berry phase. This is not surprising given that a strong spin-orbit coupling renormalizes the Landé g -factor which in turn strengthens the Zeeman-effect. We reported the same effect in WTe₂ [24].

Given the enormous, non-saturating magnetoresistance displayed by γ -MoTe₂, which is ascribed to nearly perfect electron-hole compensation [5, 22, 31], as claimed to be the case for WTe₂, we proceed by plotting its density of electron and holes as determined from Hall-effect measurements [16]. Our detailed, two-band analysis of the Hall response of γ -MoTe₂ can be found in Ref. 16. As seen in Fig. 3(a), the Hall-effect yields two important observations: two anomalies in its temperature dependence (measured under $\mu_0 H = \pm 9$ T), the first associated with the monoclinic to orthorhombic transition (indicated by the brown arrow) and the second yielding a sharp increase in the Hall constant below ~ 80 K (blue arrow) which leads to a very sharp increase in the density holes making the system almost perfectly compensated below 30 K (see Fig. 3(b)). In fact, at low temperatures the Hall resistivity is basically linear all the way up to $\mu_0 H = 9$ T indicating that γ -MoTe₂ is better compensated than WTe₂, see e.g. Ref. 25. A sharp increase in the Hall constant at lower T s is suggestive of an electronic phase-transition akin to the temperature-dependent Lifshitz-transition [32] reported for WTe₂. To evaluate this hypothesis, we performed heat capacity measurements in a β -MoTe₂ single-crystal. Figure 3(c) displays the specific heat C , normalized by the temperature and as a function of T in a logarithmic scale. C/T displays a broad anomaly around $T \simeq 66$ K roughly at the same T where one observes a sharp increase in the Hall-constant. Extrapolation to $T = 0$ K yields a sizeable electronic contribution term $\gamma_e \simeq 2.6$ mJ/mol K^2 , a surprising value for a semi-metal characterized by a relatively small density of carriers. For instance, metallic copper which contains a $\sim 10^2$ larger density of carriers yields $\gamma_e \simeq 0.69$ mJ/mol K^2 . Therefore, the large γ_e suggests a relatively high density of states at the Fermi level which is consistent with the observation of superconductivity. The broad anomaly cannot be reconciled with either a first- or a second-order phase-transition. Instead, it suggests a crossover between two regimes, and since it occurs at temperatures where C/T is dominated by phonons, it indicates the involvement of lattice degrees of freedom or that the crystallographic structure evolves upon cooling below $T = 100$ K. The Hall-effect, on the other hand, indicates that the electronic structure is affected by the evolution of the lattice upon cooling.

We investigated the temperature evolution of the crystalline-structure by performing single-crystal synchrotron X-ray diffraction measurements at low temperatures; Fig. 4 displays the lattice constants and the angles between lattice vectors as functions of the temperature

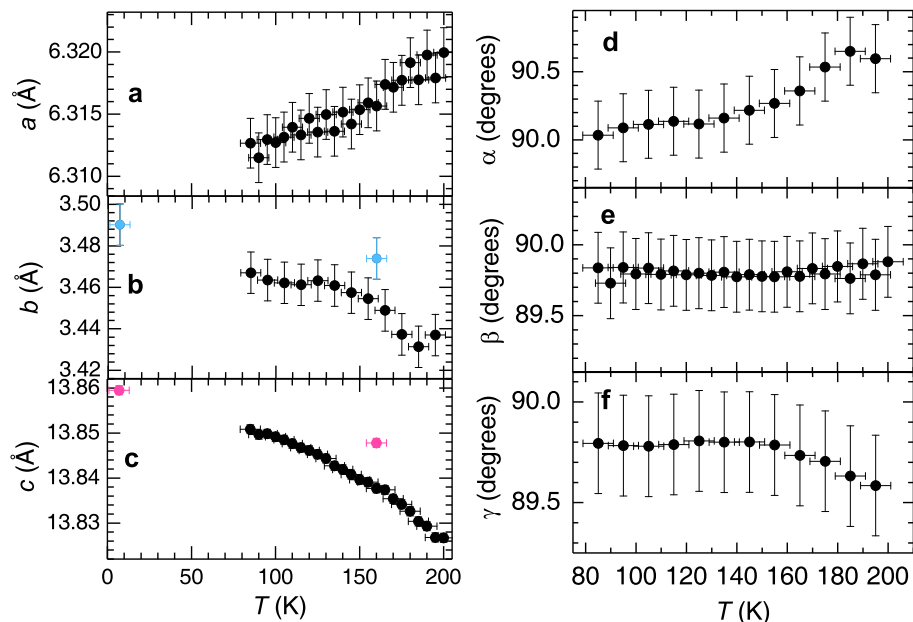


FIG. 4. (a), (b), (c) Lattice constants a , b and c of γ -MoTe₂ as functions of the temperature T . (d), (e), (f) Angles α , β and γ between the lattice vectors as functions of T . Notice that at $T = 80$ K the lattice parameters have not yet stabilized at constant values. Black markers depict sample 1, colored markers were collected from sample 2.

for $7 \text{ K} \leq T \leq 200 \text{ K}$ as collected from sample 1 (black dots) and sample 2 (colored markers). Unit cell parameters were co-refined by collecting three-dimensional center-of-mass measurements in reciprocal space of a set of 4 Bragg peaks, measured in temperature intervals of 5 K upon cooling. Notice that the lattice constants have not yet stabilized at temperatures as low as $T = 80 \text{ K}$ supporting the notion that lattice still evolves at lower temperatures. This is confirmed by sample 2: although it reveals a longer c -axis it expands considerably between $7 \text{ K} \leq T \leq 160 \text{ K}$. We also observe a major difference with respect to previous structural studies which do report the expansion of the c -axis but with mild contractions for both the a - and the b -axis [38]. Our study in both samples indicates instead that the b -axis expands considerably, by nearly $\sim 2 \%$, in this range of temperatures. Here, we have chosen the b -axis as the shorter planar lattice constant. Within the sphere of confusion of the instrument all angles between lattice vectors approach 90° as T is lowered below 150 K and as expected for an orthorhombic structure. To summarize, synchrotron X-ray diffraction confirms that the crystallographic structure of γ -MoTe₂ is temperature dependent down to quite low T s, with this compound displaying a remarkably large and negative thermal expansion coefficient along the b - and the c -axes. Notice the pronounced deviations with respect to orthorhombicity observed in the range of temperatures $150 \text{ K} \leq T \leq 250 \text{ K}$, probably a manifestation of the hysteresis associated with the structural transition at $\sim 250 \text{ K}$. In addition to lattice constants that are crystal dependent, we would like

to mention that we observe in both crystals Bragg reflections that cannot be indexed within its space-group suggesting the possibility of a super-structure. We also observe intense diffuse scattering around the Bragg reflections, indicating prominent phonon-modes. These aspects are being investigated by us and will be the subject of a subsequent report.

Since the Hall-effect points towards an evolution of the electronic structure upon cooling below 100 K, it is pertinent to ask if it considerably affects the geometry of the Fermi surface, which is the departing point of the predictions in Refs. 9–11. Figures 5(a) and 5(b) display both the de Haas van Alphen (dHvA, red traces) and the SdH signals (black traces) measured in two distinct single crystals and for two field orientations, respectively along the c - and the a -axes. As previously indicated, the dHvA and SdH signals were obtained after fitting a polynomial and subtracting it from the background magnetic torque and magnetoresistivity traces, respectively. The SdH signal was collected from a crystal displaying a $RRR \gtrsim 1000$ at $T \simeq 25 \text{ mK}$ under fields up to 18 T, while the dHvA one was obtained from a crystal displaying $RRR \gtrsim 2000$ at $T \simeq 35 \text{ mK}$ under fields up to 35 T. Both panels also display the Fast Fourier transform (FFT) of the oscillatory signal. For fields along the c -axis, one observes two main peaks at $F_\alpha = 231 \text{ T}$ and at $F_\beta = 242 \text{ T}$, as well as their first- and second harmonics and perhaps some rather small frequencies which could result from imperfect background subtraction. We obtain the same two dominant frequencies regardless of the interval in H^{-1} used to extract the

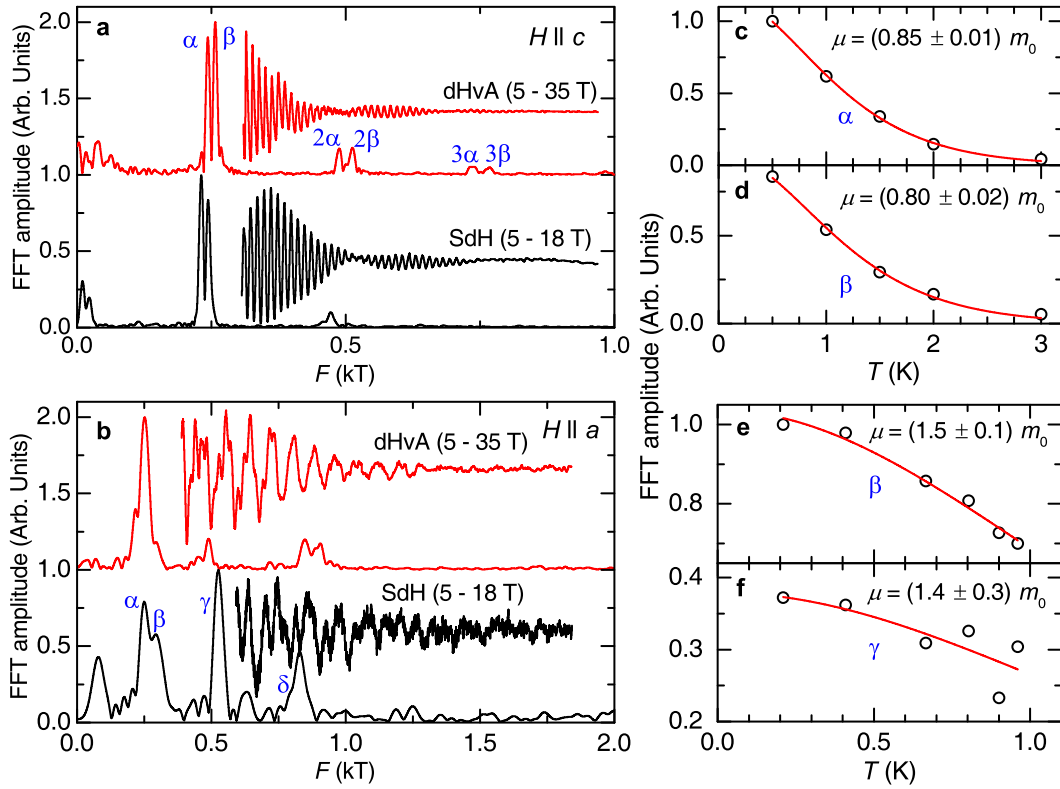


FIG. 5. (a) Typical de Haas van Alphen (red trace) and Shubnikov de Haas (black trace) signals superimposed onto the magnetic torque and the magnetoresistivity respectively, for fields aligned along the c -axis of γ -MoTe₂ single-crystals at $T \simeq 30$ mK. The same panel shows the FFT spectra for each signal revealing just two main frequencies or Fermi surface cross-sectional areas. (b) dHvA and SdH signals and corresponding FFT spectra obtained from the same single-crystals but for H aligned nearly along the a -axis of each single-crystal. (c) and (d), Amplitude of the peaks observed in the FFT spectra for $H \parallel c$ -axis and as a function of T including the corresponding fits to the LK formula from which one extracts the effective masses. (e) and (f) Amplitude of two representative peaks observed in the FFT spectra for $H \parallel a$ -axis and as a function of T with the corresponding fits to the LK formula to extract their effective masses.

FFTs. For the sake of completeness, Supplemental Fig. S2 [17] displays the dHvA signal for H aligned nearly along the b -axis along with the corresponding FFT spectra which is again dominated by two main peaks. The observation of just two main frequencies is rather surprising since, as we discuss below, Density Functional Theory (DFT) calculations, including the effect of the spin-orbit interaction performed with both the Wien2K and the VASP implementations, predict several pairs of electron-like corrugated cylindrical Fermi surfaces (FS) along with pairs of smaller three-dimensional electron-like sheets in the First-Brillouin zone. As can be seen by comparing Figs. 6 and S3 [17] there are differences in the geometry of the Fermi surface calculated *via* both implementations, but neither implementation agrees with the experiments. In addition, around the Γ -point DFT predicts at least a pair of four-fold symmetric helix-like large hole sheets. This complex Fermi surface should lead to a quite rich oscillatory signal, contrary to what is seen. One might argue that the non-observation of all of the predicted FS sheets would be attributable to an experimental lack of sensitivity or to poor sample qual-

ity which would lead to low carrier mobility. Nevertheless, our analysis of the Hall-effect within a two-carrier model [16], yields electron- and hole-mobilities ranging between 10^4 and 10^5 cm²/Vs at low T s which is consistent with both the small residual resistivities and the large resistivity ratios of our measured crystals. Given that the magnetic torque is particularly sensitive to the anisotropy of the FS, such high mobilities would have allowed us to detect the predicted FSs, particularly at the very low T s used for our measurements. Hence, we conclude that the geometry of the Fermi surface must differ considerably from the one predicted by DFT. In Figs. 5(c) and 5(d) we plot the amplitude of the main peaks observed in the FFT spectra for fields along the c -axis as a function of the temperature. Red lines are fits to the Lifshitz-Kosevich (LK) temperature damping factor, i.e. $x/\sinh x$ with $x = 14.69\mu T/H$ and with μ being the effective mass in units of the free electron mass, from which we extract the masses associated with each frequency. As seen, for $H \parallel c$ -axis one obtains $\mu_\alpha = 0.65 m_0$ and $\mu_\beta = 0.6 m_0$, which contrasts with the respective values obtained for $H \parallel a$ -axis, namely $\mu_{\alpha,\beta} \simeq 1.5$

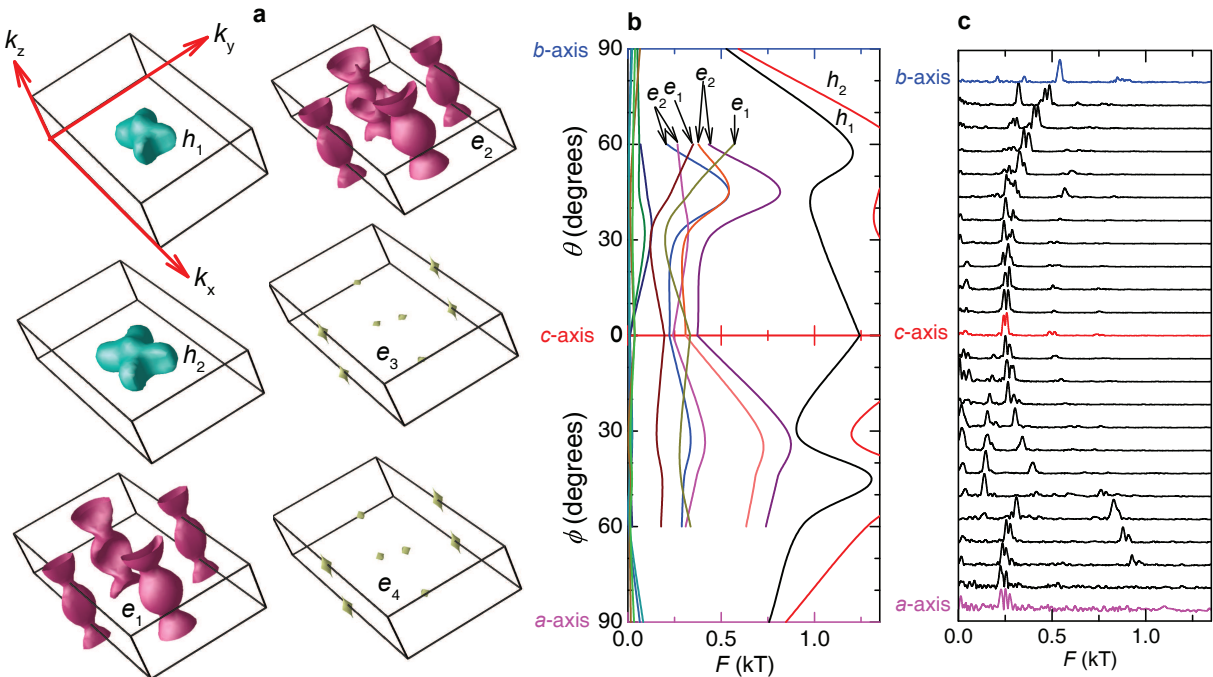


FIG. 6. (a) Fermi surface of γ -MoTe₂ as extracted from the DFT calculations using the Wien2K implementation, where the blue surfaces depict the hole sheets around the Γ -point and the purple and gray ones the electron-like surfaces in the first Brillouin zone. (b) Extremal Fermi surface cross-sectional areas obtained from the same DFT calculations as functions of the angle relative to the main crystallographic axes and in units of the cyclotron frequency. Supplementary Fig. S4 [17] shows the Fermi surface and concomitant cross-sectional areas predicted by the VASP implementation. (c) Fast Fourier transform of the dHvA signal acquired at $T \simeq 35$ mK as a function of the cyclotron frequency F and for several angles ranging from the c -axis (red trace) to the a -axis (magenta trace) and from c - to the b -axis (blue trace). The step in angle between traces is uniform throughout the panel, or $\Delta\theta \simeq 8.2^\circ$. Notice how the calculations predict far more Fermi surface cross sectional areas than the observed ones while the angular dependence of the detected frequencies, or cross-sectional areas, do not follow the angular dependence predicted by the DFT calculations.

m_0 , see Figs. 4(e) and 4(f). Therefore, γ -MoTe₂ displays a sizeable anisotropy in effective masses. A similar anisotropy is observed in WTe₂ although with a factor of ~ 2 lighter effective masses[24]. As previously mentioned, for $\mu_0 H \parallel b$ -axis we observe two main frequencies, but by reducing the H^{-1} window to focus on the higher field region, we detect additional frequencies (See, Fig. S2 [17]) which are characterized by much heavier effective masses, i.e. in the order of $4.5 m_0$. This indicates that γ -MoTe₂ displays a higher anisotropy in effective masses when compared to WTe₂, although these masses are consistent with the sizeable γ_e coefficient, suggesting that this system might be characterized by moderately strong electronic correlations.

III. DISCUSSION

Several recent angle-resolved photoemission spectroscopy (ARPES) studies [33–39] claim to find a broad agreement between the band structure calculations, the predicted geometry of the Fermi surface, the concomitant existence of Weyl type II points [9–11], and the re-

lated Fermi arcs on the surface states of γ -MoTe₂. Several of these experimental and theoretical studies claim that the electronic structure of this compound is particularly sensitive to its precise crystallographic structure. Inter-growth of the $2H$ - phase or the temperature used to collect to X -ray diffraction data, typically around 100 to 230 K, are claimed to have a considerable effect on the calculations [11, 38]. Given the few frequencies observed by us it is pertinent to ask if the low temperature evolution of the crystallographic structure unveiled here would affect the geometry of the Fermi surface of γ -MoTe₂. To address this question we performed a detailed angular-dependent study of the frequencies extracted from both the SdH and the dHvA effects in γ -MoTe₂ in order to compare with the angular dependence of the FS cross-sectional areas predicted by the calculations. In contrast to ARPES, which is a surface sensitive technique that depends upon momentum matrix elements, the magnitude of the scattering cross sections, as well as the energy and polarization of the incident light, the de Haas-van-Alphen-effect is a bulk, thermodynamic measurement which relies solely on the purity of the measured single crystals.

Figure 6(a) displays all the Fermi surface sheets predicted by DFT when using the Wien2K implementation including the spin-orbit (SO) coupling. All our calculations are based on the structure reported in Ref. 11 for the sake of comparison with both the theoretical predictions and the ARPES measurements [33–39]. See Supplemental Figs. S3, S4 and S5 [17] for, respectively, the Fermi surface obtained from the VASP implementation, the band structure and the density of states, calculated with the Wien2K implementation. The resulting four-fold symmetric SO split hole-like FS around the Γ -point, labeled as h_1 and h_2 , are depicted in blue. DFT predicts two sets of SO-split electron sheets with “crescent”-like cross sections at either side of the Γ -point as well as other two sets of SO-split surfaces around the X -point having elliptical cross-sections. We will label each subset of SO-split electron FSs as the e_1 and e_2 surfaces, respectively. Notice that the corrugation of the e_1 and e_2 surfaces leads to two extremal cross-sectional areas, i.e. “neck” and “belly” orbits. In addition, DFT predicts additional sets of small, closed SO-split electron like FSs with diamond- and ellipsoidal-like geometries, which we label as the e_3 and e_4 surfaces, respectively. Notice that different implementations the DFT method yields different geometries; this can be seen by comparing the FS in Fig. 6(a) with the one in Supplemental Fig. S3. For instance the VASP implementation yields two additional small hole-pockets at zone center with the e_1 and e_2 electron-sheets having a far more marked two dimensional character.

Figure 6 (b) plots the extreme FS cross-sectional areas that would be observed by quantum oscillatory phenomena when the field is rotated within the $a - b$ and $a - c$ planes. In this plot the Onsager relation was used to convert the cross-sectional areas into oscillatory phenomena frequencies. θ refers to angles between the c - and the a -axis, where $\theta = 0^\circ$ corresponds to $H \parallel c$ -axis, while ϕ corresponds to angles between the c - and the b -axis, again relative to the c -axis. As seen, all closed electron orbits, namely e_3 and e_4 , should yield frequencies well below 100 T, while the open ones that is e_1 and e_2 , should yield frequencies ranging from 200 to 400 T for angles close to the c -axis. Since e_1 and e_2 are open FS sheets, for angles beyond 60° their related orbits diverge as one approaches either the a - or the b -axis (see, Supplemental Fig. S3). Finally, h_1 and h_2 should yield frequencies in excess of 1 kT for $H \parallel c$ -axis, which decrease to values ranging between 0.5 and 0.85 kT for fields along the other two axes. Figure 6(c) displays the FFT spectra of the dHvA signal (see the oscillatory signal in the Supplemental Fig. S6 [17]) as a function of the cyclotron frequency F . As previously discussed, for $H \parallel c$ -axis the FFT spectra is dominated by a double peak structure centered around 250 T which is in the range of frequencies predicted for the orbits on the e_1 and e_2 surfaces. One also detects its first and second harmonics and an additional small frequency around 30 T which is close to the frequencies predicted for the small electron-like ellipsoids

on the e_3 and e_4 surfaces. However, as the field is rotated towards either the a - or the b -axis, it splits while yielding finite frequencies along both axes. This indicates unambiguously that the related Fermi surfaces are closed, or are of three-dimensional in character, in sharp contrast with the DFT calculations that predicts corrugated cylinders. Furthermore, their angular dependence differs considerably from the one predicted by DFT for the e_1 and e_2 surfaces. These observations, coupled to the non-detection of all of the predicted orbits, in particular the large hole h_1 and h_2 Fermi surfaces, indicate unambiguously that the geometry of Fermi surface of γ -MoTe₂ is very different from the calculated one. Notice that according to ARPES the Weyl type-II points would result from touchings between the e_2 electron- and the h_2 hole-like Fermi surface sheets [33–38]. These FS sheets were not observed in the present study, despite the very high mobility of these samples, the very high magnetic fields and the ultra-low temperatures used for this study, indicating their non-existence. Such a discrepancy between DFT and quantum oscillatory phenomena is not surprising given that a similar discrepancy is also observed in its isostructural WTe₂ compound whose FSs are simple ellipsoids in contrast to the calculations [24, 31]. However, the geometry of the observed FS sheets of γ -MoTe₂ cannot be described in terms of ellipsoids. To summarize, our experimental study does not support the notion of γ -MoTe₂ being a Weyl type-II semi-metal.

IV. CONCLUSIONS

In conclusion, quantum oscillatory phenomena indicates that one should be careful concerning the claims of a broad agreement between the calculations and the geometry of the Fermi surface of γ -MoTe₂ as revealed by ARPES measurements [33–38]. To understand this disagreement one should consider that the Fermi surfaces predicted by density functional theory calculations for semi-metallic systems, which are characterized by small Fermi surfaces, are extremely sensitive to the exact position of the Fermi level E_F or the strength of the inter-planar coupling in layered, van der Waals-like, compounds as γ -MoTe₂. Small displacements in E_F alter considerably the geometry and even the number of Fermi sheets [24]. On the other hand, as illustrated by the Fermi surface [24] of WTe₂ and the present work, DFT tends to underestimate the coupling between the planes in layered systems, pointing to two-dimensional Fermi surfaces when in reality they are closed or three-dimensional in character. In general, these systems are weakly and not really van der Waals coupled; the electronic bands do disperse along the inter-layer direction. As for ARPES, traditionally it tends to disagree with quantum oscillatory phenomena: for example, the Fermi surface of Sr₂RuO₄, as extracted from a detailed analysis of the de Haas van Alphen effect [40], differs considerably from the one originally extracted by ARPES

[41]. ARPES observes Fermi arcs [42] in the underdoped cuprates when quantum oscillatory phenomena observes Fermi surface pockets [43]. In contrast to quantum oscillatory phenomena ARPES relies on DFT to interpret its spectra, which might introduce a certain bias. It is very difficult to conceive that a high sensitivity thermodynamic and thus bulk technique would yield the incorrect Fermi surface geometry while a surface technique, with far more limited resolution and a particular sensitivity to surface states and surface polarizability, would provide the correct one. Nevertheless, notice that an ARPES study performed in γ - $\text{Mo}_{1-x}\text{W}_x\text{Te}_2$ alloys, within the Mo rich region of the phase-diagram as a function of x , yields a Fermi surface in far better agreement with our quantum oscillatory measurements [44].

We ascribe the discrepancy between the calculated Fermi surfaces and those detected via quantum oscillatory phenomena to: i) the evolution of the crystallographic structure of γ - MoTe_2 upon cooling below 100 K as indicated by both the heat-capacity and the synchrotron single-crystal X-ray data, ii) a possible electronic phase-transition upon cooling as suggested by the Hall-effect (perhaps leading to the superstructures observed by X-ray) and iii) limitations of the current DFT methods to capture the strength of the inter-planar coupling in weakly-coupled layered systems as well as the exact position of the Fermi level. This last aspect is illustrated by the differences in the geometry of the

Fermi surface of γ - MoTe_2 produced by the VASP and Wien2K implementations of the DFT method included here. Needless to say that the correct low-temperature crystallographic and electronic structures of γ - MoTe_2 are of paramount importance for unveiling its possible topological character, for determining its superconducting pairing symmetry or the reason for the sensitivity of T_c with respect to structural disorder.

ACKNOWLEDGMENTS

[†]These authors contributed equally to this work. We acknowledge helpful discussions with R. M. Osgood and A. N. Pasupathy. G.T.M. and J.Y.C. are supported by NSF-DMR-1360863. L. B. is supported by DOE-BES through award de-sc0002613 for experiments under high magnetic fields and at very low temperatures, and by the U.S. Army Research Office MURI Grant W911NF-11-1-0362 for the synthesis and physical characterization of two-dimensional materials and their heterostructures. We acknowledge the support of the HLD-HZDR, member of the European Magnetic Field Laboratory (EMFL). Research conducted at the Cornell High Energy Synchrotron Source (CHESS) is supported by the NSF & NIH/NIGMS via NSF award DMR-1332208. The NHMFL is supported by NSF through NSF-DMR-1157490 and the State of Florida.

-
- [1] X. F. Qian, J. W. Liu, L. Fu, and J. Li, *Quantum spin Hall effect in two-dimensional transition metal dichalcogenides*, Science **346**, 1344 (2014).
 - [2] D. Pesin, and A. H. MacDonald, *Spintronics and pseudospintronics in graphene and topological insulators*, Nat. Mater. **11**, 409-416 (2012).
 - [3] M. Chhowalla, H. S. Shin, G. Eda, L. -J. Li, K. P. Loh, and H. Zhang, *The chemistry of two-dimensional layered transition metal dichalcogenide nanosheets*, Nat. Chem. **5**, 263-275 (2013).
 - [4] S. Z. Butler, S. M. Hollen, L. Cao, Y. Cui, J. A. Gupta, H. R. Gutiérrez, T. F. Heinz, S. S. Hong, J. Huang, A. F. Ismach, E. Johnston-Halperin, M. Kuno, V. V. Plashnitsa, R. D. Robinson, R. S. Ruoff, S. Salahuddin, J. Shan, L. Shi, M. G. Spencer, M. Terrones, W. Windl and J. E. Goldberger, *Progress, Challenges, and Opportunities in Two-Dimensional Materials Beyond Graphene*, ACS Nano **7**, 2898-2926 (2013).
 - [5] M. N. Ali, J. Xiong, S. Flynn, J. Tao, Q. D. Gibson, L. M. Schoop, T. Liang, N. Haldolaarachchige, M. Hirschberger, N. P. Ong and R. J. Cava, *Large, non-saturating magnetoresistance in WTe_2* , Nature **514**, 205-208 (2014).
 - [6] D. H. Keum, S. Cho, J. H. Kim, D. -H. Choe, H. -J. Sung, M. Kan, H. Kang, J. -Y. Hwang, S. W. Kim, H. Yang, K. J. Chang and Y. H. Lee, *Bandgap opening in few-layered monoclinic MoTe_2* , Nat. Phys. **11**, 482-486 (2015).
 - [7] H. Y. Lv, W. J. Lu, D. F. Shao, Y. Liu, S. G. Tan, and Y. P. Sun, *Perfect charge compensation in WTe_2 for the extraordinary magnetoresistance: From bulk to monolayer*, EPL **110**, 37004 (2015).
 - [8] L. Wang, I. Gutiérrez-Lezama, C. Barreteau, N. Ubrig, E. Giannini, and A. F. Morpurgo, *Tuning magnetotransport in a compensated semimetal at the atomic scale*, Nat. Commun. **6**, 8892 (2015).
 - [9] A. A. Soluyanov, D. Gresch, Z. Wang, Q. Wu, M. Troyer, X. Dai and B. A. Bernevig, *A New Type of Weyl Semimetals*, Nature **527**, 495-498 (2015).
 - [10] Y. Sun, S.C. Wu, M. N. Ali, C. Felser, and B. Yan, *Prediction of the Weyl semimetal in the orthorhombic MoTe_2* , Phys. Rev. B **92**, 161107 (2015).
 - [11] Z. Wang, D. Gresch, A. A. Soluyanov, W. Xie, S. Kushwaha, X. Dai, M. Troyer, R. J. Cava, and B. A. Bernevig, *MoTe_2 : A Type-II Weyl Topological Metal*, Phys. Rev. Lett. **117**, 056805 (2016).
 - [12] H. M. Weng, C. Fang, Z. Fang, B. A. Bernevig, and X. Dai, *Weyl Semimetal Phase in Noncentrosymmetric Transition-Metal Monophosphides*, Phys. Rev. X **5**, 011029 (2015).
 - [13] S. Y. Xu, I. Belopolski, N. Alidoust, M. Neupane, G. Bian, C. Zhang, R. Sankar, G. Chang, Z. Yuan, C. -C. Lee, S. -M. Huang, H. Zheng, J. Ma, D. S. Sanchez, B. Wang, A. Bansil, F. Chou, P. P. Shibayev, H. Lin, S. Jia, M. Z. Hasan, *Discovery of a Weyl fermion semimetal and topological Fermi arcs*, Science **349**, 613-617 (2015).
 - [14] T. R. Chang, S. -Y. Xu, G. Chang, C. -C. Lee, S. -M. Huang, B. Wang, G. Bian, H. Zheng, D. S. Sanchez, I. Belopolski, N. Alidoust, M. Neupane, A. Bansil, H. -T.

- Jeng, H. Lin, and M. Z. Hasan, *Prediction of an arc-tunable Weyl Fermion metallic state in $\text{Mo}_x\text{W}_{1-x}\text{Te}_2$* , Nat. Commun. **7**, 10639 (2016).
- [15] Y. Qi, P. G. Naumov, M. N. Ali, C. R. Rajamathi, W. Schnelle, O. Barkalov, M. Hanfland, S. -C. Wu, C. Shekhar, Y. Sun, V. Süß, M. Schmidt, U. Schwarz, E. Pippel, P. Werner, R. Hillebrand, T. Förster, E. Kampert, S. Parkin, R. J. Cava, C. Felser, B. Yan and S. A. Medvedev, *Superconductivity in Weyl semimetal candidate MoTe_2* , Nat. Commun. **7**, 11038 (2016).
- [16] Q. Zhou, D. Rhodes, Q. R. Zhang, S. Tang, R. Schönemann, and L. Balicas, *Hall effect within the colossal magnetoresistive semimetallic state of MoTe_2* , Phys. Rev. B **94**, 121101(R) (2016).
- [17] See supplemental material at <http://link.aps.org/>
- [18] A. P. Mackenzie, R. K. W. Haselwimmer, A. W. Tyler, G. G. Lonzarich, Y. Mori, S. Nishizaki, and Y. Maeno, *Extremely strong dependence of superconductivity on disorder in Sr_2RuO_4* , Phys. Rev. Lett. **80**, 161-164 (1998).
- [19] S. Nakatsuji, K. Kuga, Y. Machida, T. Tayama, T. Sakakibara, Y. Karaki, H. Ishimoto, S. Yonezawa, Y. Maeno, E. Pearson, G. G. Lonzarich, L. Balicas, H. Lee and Z. Fisk, *Superconductivity and quantum criticality in the heavy-fermion system $\beta\text{-YbAlB}_4$* , Nat. Phys. **4**, 603-607 (2008).
- [20] M. Tsujimoto, Y. Matsumoto, T. Tomita, A. Sakai, S. Nakatsuji, *Heavy-Fermion Superconductivity in the Quadrupole Ordered State of $\text{PrV}_2\text{Al}_{20}$* , Phys. Rev. Lett. **113**, 267001 (2014).
- [21] A. P. Mackenzie, and Y. Maeno, *The superconductivity of Sr_2RuO_4 and the physics of spin-triplet pairing*, Rev. Mod. Phys. **75**, 657-712 (2003).
- [22] I. Pletikosić, M. N. Ali, A. V. Fedorov, R. J. Cava, and T. Valla, *Electronic Structure Basis for the Extraordinary Magnetoresistance in WTe_2* , Phys. Rev. Lett. **113**, 216601 (2014).
- [23] A. B. Pippard, *Magnetoresistance in Metals* (Cambridge University, Cambridge, 1989).
- [24] D. Rhodes, S. Das, Q. R. Zhang, B. Zeng, N. R. Pradhan, N. Kikugawa, E. Manousakis, and L. Balicas, *Role of spin-orbit coupling and evolution of the electronic structure of WTe_2 under an external magnetic field*, Phys. Rev. B **92**, 125152 (2015).
- [25] Y. Luo, H. Li, Y. M. Dai, H. Miao, Y. G. Shi, H. Ding, A. J. Taylor, D. A. Yarotski, R. P. Prasankumar, and J. D. Thompson, *Hall effect in the extremely large magnetoresistance semimetal WTe_2* , Appl. Phys. Lett. **107**, 182411 (2015).
- [26] D. Kang, Y. Zhou, W. Yi, C. Yang, J. Guo, Y. Shi, S. Zhang, Z. Wang, C. Zhang, S. Jiang, A. Li, K. Yang, Q. Wu, G. Zhang, L. Sun and Z. Zhao *Superconductivity emerging from a suppressed large magnetoresistant state in tungsten ditelluride*, Nat. Commun. **6**, 7804 (2015).
- [27] Y. L. Wang, K. F. Wang, J. Reutt-Robey, J. Paglione, and M. S. Fuhrer, *Breakdown of compensation and persistence of nonsaturating magnetoresistance in gated WTe_2 thin flakes*, Phys. Rev. B **93**, 121108 (2016).
- [28] Y. B. Zhang, Y. W. Tan, H. L. Stormer, P. Kim, *Experimental observation of the quantum Hall effect and Berry's phase in graphene*, Nature **438**, 201-204 (2005).
- [29] H. Murakawa, M. S. Bahramy, M. Tokunaga, Y. Kohama, C. Bell, Y. Kaneko, N. Nagaosa, H. Y. Hwang, Y. Tokura, *Detection of Berry's Phase in a Bulk Rashba Semiconductor*, Science **342**, 1490-1493 (2013).
- [30] I. A. Luk'yanchuk, and Y. Kopelevich, *Phase Analysis of Quantum Oscillations in Graphite*, Phys. Rev. Lett. **93**, 166402 (2004).
- [31] Z. Zhu, X. Lin, J. Liu, B. Fauqué, Q. Tao, C. Yang, Y. Shi, and K. Behnia, *Quantum Oscillations, Thermoelectric Coefficients, and the Fermi Surface of Semimetallic WTe_2* , Phys. Rev. Lett. **114**, 176601 (2015).
- [32] Y. Wu, N. H. Jo, M. Ochi, L. Huang, D. Mou, S. L. Bud'ko, P. C. Canfield, N. Trivedi, R. Arita, and A. Kaminski, *Temperature induced Lifshitz transition in WTe_2* , Phys. Rev. Lett. **115**, 166602 (2015).
- [33] L. Huang, T. M. McCormick, M. Ochi, Z. Zhao, M. -T. Suzuki, R. Arita, Y. Wu, D. Mou, H. Cao, J. Yan, N. Trivedi, and A. Kaminski, *Spectroscopic evidence for type II Weyl semimetal state in MoTe_2* , Nat. Mater. **15**, 1155-1160 (2016).
- [34] K. Deng, G. Wan, P. Deng, K. Zhang, S. Ding, E. Wang, M. Yan, H. Huang, H. Zhang, Z. Xu, J. Denlinger, A. Fedorov, H. Yang, W. Duan, H. Yao, Y. Wu, S. Fan, H. Zhang, X. Chen and S. Zhou, *Experimental observation of topological Fermi arcs in type-II Weyl semimetal MoTe_2* , Nat. Phys. **12**, 1105 (2016).
- [35] J. Jiang, Z. K. Liu, Y. Sun, H. F. Yang, R. Rajamathi, Y. P. Qi, L. X. Yang, C. Chen, H. Peng, C. -C. Hwang, S. Z. Sun, S. -K. Mo, I. Vobornik, J. Fujii, S. S. P. Parkin, C. Felser, B. H. Yan, Y. L. Chen, *Observation of the Type-II Weyl Semimetal Phase in MoTe_2* , arXiv:1604.00139 (2016).
- [36] A. Liang, J. Huang, S. Nie, Y. Ding, Q. Gao, C. Hu, S. He, Y. Zhang, C. Wang, B. Shen, J. Liu, P. Ai, L. Yu, X. Sun, W. Zhao, S. Lv, D. Liu, C. Li, Y. Zhang, Y. Hu, Y. Xu, L. Zhao, G. Liu, Z. Mao, X. Jia, F. Zhang, S. Zhang, F. Yang, Z. Wang, Q. Peng, H. Weng, X. Dai, Z. Fang, Z. Xu, C. Chen, X. J. Zhou, *Electronic Evidence for Type II Weyl Semimetal State in MoTe_2* , arXiv:1604.01706 (2016).
- [37] N. Xu, Z. J. Wang, A. P. Weber, A. Magrez, P. Bugnon, H. Berger, C. E. Matt, J. Z. Ma, B. B. Fu, B. Q. Lv, N. C. Plumb, M. Radovic, E. Pomjakushina, K. Conder, T. Qian, J. H. Dil, J. Mesot, H. Ding, M. Shi, *Discovery of Weyl semimetal state violating Lorentz invariance in MoTe_2* , arXiv:1604.02116 (2016).
- [38] A. Tamai, Q. S. Wu, I. Cucchi, F. Y. Bruno, S. Ricco, T. K. Kim, M. Hoesch, C. Barreteau, E. Giannini, C. Bernard, A. A. Soluyanov, F. Baumberger, *Fermi arcs and their topological character in the candidate type-II Weyl semimetal MoTe_2* , Phys. Rev. X **6**, 031021 (2016), and references therein.
- [39] I. Belopolski, D. S. Sanchez, Y. Ishida, X. C. Pan, P. Yu, S. Y. Xu, G. Q. Chang, T. R. Chang, H. Zheng, N. Alidoust, G. Bian, M. Neupane, S. M. Huang, C. C. Lee, Y. Song, H. Bu, G. Wang, S. Li, G. Eda, H.-T. Jeng, T. Kondo, H. Lin, Z. Liu, F. Song, S. Shin and M. Z. Hasan, *Discovery of a new type of topological Weyl fermion semimetal state in $\text{Mo}_x\text{W}_{1-x}\text{Te}_2$* , Nat. Commun. **7**, 13643 (2016).
- [40] C. Bergemann, A. P. Mackenzie, S. R. Julian, D. Forsythe, and E. Ohmich, *Quasi-two-dimensional Fermi liquid properties of the unconventional superconductor Sr_2RuO_4* , Adv. Phys. **52**, 639-725 (2003).
- [41] D. H. Lu, M. Schmidt, T. R. Cummins, S. Schuppler, F. Lichtenberg and J. G. Bednorz, *Fermi Surface and Extended van Hove Singularity in the Noncuprate Superconductor Sr_2RuO_4* , Phys. Rev. Lett. **76**, 4845 (1996).

- [42] M. R. Norman, H. Ding, M. Randeria, J. C. Campuzano, T. Yokoya, T. Takeuchi, T. Takahashi, T. Mochiku, K. Kadowaki, P. Guptasarma, and D. G. Hinks, *Destruction of the Fermi surface in underdoped high- T_c superconductors*, Nature **392**, 157-160 (1998).
- [43] N. Doiron-Leyraud, C. Proust, D. LeBoeuf, J. Levallois, J. B. Bonnemaïson, R. X. Liang, D. A. Bonn, W. N. Hardy, and L. Taillefer, *Quantum oscillations and the Fermi surface in an underdoped high- T_c superconductor*, Nature **447**, 565-568 (2007).
- [44] D. Rhodes, D. A. Chenet, B. E. Janicek, C. Nyby, Y. Lin, W. Jin, D. Edelberg, E. Mannebach, N. Finney, A. Antony, T. Schiros, T. Klarr, A. Mazzoni, M. Chin, Y.-c. Chiu, W. Zheng, Q. R. Zhang, F. Ernst, J. I. Dadap, X. Tong, J. Ma, R. Lou, S. Wang, T. Qian, H. Ding, R. M. Osgood, Jr, D. W. Paley, A. M. Lindenberg, P. Y. Huang, A. N. Pasupathy, M. Dubey, J. Hone, and L. Balicas, *Engineering the structural and electronic phases of MoTe_2 through W substitution*, Nano Lett. **17**, 1616 (2017).